

PAPER

Langmuir probe characterisation of an Ar-H₂ non-thermal plasma loaded with carbon nanoparticles

To cite this article: Austin Woodard *et al* 2018 *Plasma Sources Sci. Technol.* **27** 104003

View the [article online](#) for updates and enhancements.



IOP | ebooks™

Bringing you innovative digital publishing with leading voices to create your essential collection of books in STEM research.

Start exploring the [collection](#) - download the first chapter of every title for free.

Langmuir probe characterisation of an Ar–H₂ non-thermal plasma loaded with carbon nanoparticles

Austin Woodard¹, Kamran Shojaei², Giorgio Nava² and Lorenzo Mangolini^{1,2} 

¹ Materials Science & Engineering Program, University of California Riverside, Riverside, CA, United States of America

² Department of Mechanical Engineering, University of California Riverside, Riverside, CA, United States of America

E-mail: lmangolini@engr.ucr.edu

Received 14 May 2018, revised 20 August 2018

Accepted for publication 17 September 2018

Published 15 October 2018



Abstract

In this contribution, we describe the development of a test-bed for the characterisation of non-thermal dusty plasmas via Langmuir probe. This technique, while allowing the precise determination of plasma parameters and electron energy distribution function (EEDF), is notoriously difficult to apply in dust-forming chemistries. We overcome this limitation by utilising a two-plasmas system in which the particle precursor, in this case acetylene, is fully consumed and converted into nanoparticles in a first plasma reactor, followed by the injection of the dust into a second plasma reactor where the Langmuir probe measurement is performed. This approach allows studying the influence of the variation of process parameters on the dusty plasma properties, all while leaving the nucleation and growth phase of the particles unaffected and fully decoupled from the discharge in which the measurement takes place. We have applied this approach to the case of graphitic carbon nanoparticles dispersed in an argon–hydrogen mixture. We have monitored the quality of the Langmuir probe measurement, and found that it is minimally affected by the presence of the graphitic particles even after several EEDF measurements. Our measurements confirm the unipolar charging of nanoparticles in non-thermal plasmas, consistent with previous observations and theoretical predictions. We also observe an unexpected trend with plasma input power: the charge carried by the particles does not monotonically increase with increased power, instead starts decreasing at sufficiently high input power levels.

Keywords: Langmuir probe, dusty plasma, non-thermal plasma, graphitic carbon nanoparticles

1. Introduction

Low-temperature gas discharges are widely employed in several industrial manufacturing processes, such as thin-film deposition, material functionalization and etching. The formation of particles represents an ever-present issue in processing plasmas, and the investigation of particle-related phenomena led to the genesis of what we call ‘science of dusty-plasmas’. The formation of particulate in a plasma discharge, at first regarded merely as problem to be tackled [1, 2], has been later investigated as a possible route for the

controlled fabrication of nanopowders. Non-thermal plasma processes have been successfully optimised for the deliberate formation of nanoparticles, as confirmed by several reports on the non-thermal plasma synthesis of high quality nanocrystals composed of a broad range of materials [3, 4]. These methods are attracting a growing interest, possibly representing a key enabler for the future large-scale utilisation of various nanoarchitectures in plasmonic [5, 6], thermoelectrics [7], microelectronics [8–10] and energy-storage applications [11–13]. Unveiling the fundamental physics and properties of dusty discharges clearly represents a crucial requirement to

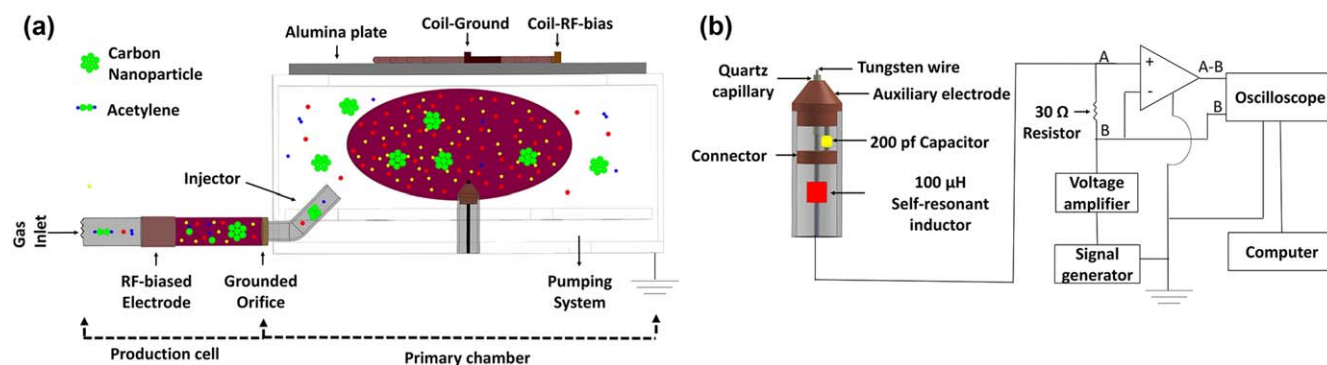


Figure 1. (a) Schematic of the system showing nanoparticle production cell, nanoparticle injection system and the primary chamber. (b) Schematic of the probe design and measurement system.

gain a better understanding of all the aforementioned plasma-based systems and contribute to their engineering and optimisation. Among several plasma characterisation techniques, the Langmuir probe method represents one of the most established measurement routines.

The in-depth analysis of the probe current–voltage characteristics provides detailed information regarding the ion and electron densities, the electron temperature and the electron energy distribution function (EEDF) [14–16]. The method has been widely adopted across industrial plasmas for the real-time monitoring of the plasma characteristics and the tuning of the operating conditions. In dust-forming plasmas, however, the application of the Langmuir probe measurement remains a challenging endeavour. The growth of insulating films over the probe surface severely affects the reliability of the measurement. The successful application of the Langmuir probe method in a dusty plasma requires substantial modifications of the probe design and elaborate measurement strategies to tackle issues related to particle formation. For instance, Bilik *et al* [17] have developed a shielded Langmuir probe technique to measure the EEDF in a low-pressure silane-containing plasma, and successfully monitored its evolution during the nucleation and growth of silicon particles. In this study, the probe is isolated from the plasma via a retractable ceramic shield during most of the process, and exposed to the plasma only during brief periods of time to perform the I – V measurement. This ingenious, while non-trivial, approach is therefore applied to the complex scenario in which the precursor is continuously supplied to the plasma volume in which the probe is inserted, with particle nucleation and growth, together with growth of a thin-film via CVD, also continuously occurring. In our contribution, we present a simpler approach based on a standard Langmuir probe measurement to successfully investigate the relation between plasma properties and the introduction of nanoparticles into a non-thermal low-pressure discharge. A radio frequency (RF) argon–hydrogen—Ar–H₂—plasma is generated in a primary reactor with a planar-coil inductive source. The reactor is controllably dosed with conductive graphitic carbon nanoparticles produced in a secondary RF Ar–H₂ plasma from the dissociation of acetylene—C₂H₂. This allows decoupling the particle nucleation phase from the plasma in which the measurement is performed, since the precursor is fully

converted into nanoparticles in the nanoparticle-producing plasma. As a consequence, this approach offers a pathway towards investigating the effect of common process parameters, such as pressure, gas composition, electrical input power, on a dusty plasma which is controllably and consistently dosed with the same particles, in terms of their composition, size and density. We have found that the use of graphitic nanoparticles, in combination with the elimination of the CVD film growth on the probe tip (the precursor is fully consumed in the nanoparticle-producing step), allows for a measurement environment that is substantially more forgiving to the Langmuir probe technique. No changes were observed in the EEDF measured for a pristine plasma before and after several measurements performed in the dusty plasma regime. For this study, we focus on the effect of primary plasma RF power on plasma properties in the dust-rich conditions. As expected from theory and previous literature, nanoparticles act as electron sinks, reducing the electron density inside the plasma volume and severely affecting the power coupling. The number of charges per nanoparticle is derived across the space of the investigated plasma parameters by monitoring the deficit between ion and electron densities. Notably, the particle charge has been found not to increase monotonically with plasma density. It decreases for high input plasma power.

2. Experimental setup

Figure 1(a) depicts the system used in the experiments. The primary reactor consists of a cylindrical stainless-steel vacuum chamber covered by a circular alumina plate (diameter 32 cm and thickness 1 cm) with a grounded Faraday shield and connected to a Leybold TURBOVAC SL80 turbopump. The Ar–H₂ is produced in the primary chamber with a three-turn planar coil. The secondary reactor—nanoparticle production cell—comprises a 2.54 cm diameter quartz tube reactor with a copper ring electrode and a grounded 2 mm orifice. The system is designed to inject the produced particles in the centre of the primary plasma. The gas mixture supplied through the nanoparticle production cell comprises of 28 sccm of Ar, 0.6 sccm of H₂ and 0.28 sccm of acetylene (C₂H₂). We have performed extensive residual gas analyser

measurements confirming that the nanoparticle precursor (acetylene) is fully converted to nanoparticles during the nanoparticle production step. The RF power supplied to the first plasma is 70 W. The pressure in the nanoparticle-producing plasma is 2.3 Torr, while the pressure in the primary chamber is 150 mTorr. The mass production rate of the carbon nanoparticles was determined by collecting the synthesised material on stainless-steel mesh for 2 h and measuring the mass of the deposit with a Sartorius ENTRIS64-1S microbalance. TEM analysis was performed on the synthesised material on a Tecnai12. The particle size distribution, the average nanoparticle size and the standard deviation were obtained from the measurement of an ensemble of 100 nanoparticles using ImageJ software. The Raman spectrum of the carbon nanoparticles was acquired with a Raman Horiba LabRam microscope (spectral range 400–4000 cm^{-1} , laser wavelength 532 nm, laser power 0.06 mW, objective 50 \times).

The powered-electrodes of the primary and secondary reactors are connected to independently controlled RF generators through an L-type matching network. In this work, the power values reported for the primary plasma refer to the actual power coupled into the discharge which is calculated with the following procedure:

1. The desired gas mixture is flowed into the primary reactor and the desired RF power is supplied while tuning the matching network to minimise reflected power.
2. The net power (forward minus reflected), and the rms current through the planar-coil, which is measured with a Pearson 2877 current probe, are recorded.
3. The system is evacuated at its base pressure, typically around 10^{-6} Torr.
4. The RF power is again supplied to the reactor without striking a discharge. Power is adjusted to match the rms current measured in point 2. The new net power (forward minus reflected) is recorded. This value represents the losses due to joule heating and radiation through the coil and the matching network.
5. The actual power is calculated as the difference between the net powers measured in point 2 and point 4.

Figure 1(b) depicts Langmuir probe and the measurement system employed for the acquisition of the I – V characteristics. The Langmuir probe is positioned in the centre of the primary reactor along a line perpendicular to the plane of the coil. The distance between the bottom of the alumina plate and the probe tip is 4 cm. Tungsten wire was used for the probe material, with an exposed tip length of 5 mm and tip diameter of 127 μm . The Langmuir probe employs a self-compensated design [18, 19], with a large area auxiliary electrode and a 200 pF capacitor. A self-resonating 100 μH inductor—set to the 13.56 MHz frequency used for the RF power source—is inserted in series with the probe to eliminate RF disturbances to the probe signal and development of RF across the probe. A Fourier transform on the current through the probe, with the plasma on, suggests that this design reduces the RF harmonics below the detection limit of our current setup.

The sweeping voltage (B in figure 1(b)) required for Langmuir probe measurements is provided by a Wavetek 182 signal generator pushing a triangular wave at 10 Hz which is amplified using a Kepco BOP 100-1M. The probe current is monitored by measuring the potential drop across a 30 Ω resistor. A Teledyne DA1855A differential amplifier is used to measure this voltage drop. The signals are recorded with a PicoScope 5442A digital oscilloscope performing a weighted average over 667 waveforms with an ultimate time-to-measure of three minutes per I – V curve. The Langmuir probe measurement routine is the following:

1. The whole system is evacuated at a base pressure of 10^{-6} Torr.
2. The Ar–H₂ gas mix is flowed into the system and a plasma discharge is ignited in the primary reactor.
3. The I – V characteristic of the Langmuir probe is acquired in dust-free conditions.
4. The whole system is evacuated at a base pressure of 10^{-6} Torr.
5. The Ar–H₂–C₂H₂ gas admixture is flowed into the system. The discharge is ignited in both the secondary reactor, hence starting the production of graphitic particles, and in the primary reactor. I – V characteristics are measured under dusty conditions while varying the desired parameter, such as input power.
6. The system is again evacuated down to a base pressure of 10^{-6} Torr. Point 2 and point 3 are repeated.
7. The EEDFs derived from 3 and 6 are compared to ensure that effects arising from the accumulation of graphitic nanoparticles at the probe tip are negligible.

As a precautionary measure, the probe tip is restored to pristine condition by applying a sufficiently positive bias for 10 s to lead to visible glowing of the probe tip. The process, induced by Joule heating at the probe tip, effectively removes any deposit from the probe surface.

The current and voltage waveforms are smoothed via Savitzky–Golay averaging. Following the Druyvesteyn method [20], both the EEDF, $F(E)$, and the electron energy probability function, $f(E)$, are determined from the measured I – V from the equation described in (1) and (2):

$$F(E) = \frac{\sqrt{8m_e}}{e^3 A_p} \sqrt{E} \frac{dI_e^2}{d^2|V_p - V|}, \quad (1)$$

$$f(E) = \frac{F(E)}{\sqrt{E}}, \quad (2)$$

where E is the energy, m_e the mass of an electron, e the charge of an electron, A_p the area of the probe surface, I_e the electron current, V_p the plasma potential, and V the sweeping voltage applied to the probe tip. The plasma potential V_p corresponds to the inflection point in the I – V characteristic. Additional adjacent averaging is performed on the second derivative to obtain $F(E)$. The electron— n_e —and ion— n_{ion} —densities, electron temperature— T_e —and the particle charge— Q —were calculated from $F(E)$ using the equations (3)–(6):

$$n_e = \int_0^\infty F(E) dE, \quad (3)$$

$$n_{\text{ion}} = \frac{I_{\text{ion}}}{2eR_pL_p\sqrt{\frac{2e|V_p - V|}{m_{\text{ion}}}}}, \quad (4)$$

$$T_e = \frac{2}{3}n_e^{-1} \int_0^\infty EF(E)dE, \quad (5)$$

$$Q = \frac{n_{\text{ion}} - n_e}{n_{\text{particle}}}, \quad (6)$$

where R_p and L_p are the probe tip radius and length respectively, m_{ion} is the mass of an ion and n_{particle} is the particle density in the plasma.

3. Results

In the nanoparticle generation cell, the production parameters were optimised to give graphitic particles. This structure, due to its higher electrical conductivity as compared to, for instance, amorphous carbon, minimises the perturbation in the Langmuir probe measurement resulting from dust accumulation at the probe tip. More details about the process employed for the fabrication of the carbon nanoparticles and the mechanism leading to their graphitisation in the plasma environment are reported in our previous publication [21]. The carbonaceous nanomaterials produced in the secondary reactor were collected and characterised via TEM and Raman spectroscopy. The results are detailed in figure 2. Nanoparticles with a collapsed-graphene morphology (see figure 2(a)) and a fairly monodisperse particle size distribution (see figure 2(b)), with an average diameter 14 nm and standard deviation 1.7 nm, are observed from the TEM scans. The corresponding Raman spectrum (see figure 2(c)) shows two sharp peaks around 1330 cm^{-1} and 1610 cm^{-1} , the D and G modes respectively, and three smaller but still well-visible features around 2650 cm^{-1} , 2900 cm^{-1} and 3200 cm^{-1} , the second order D', D'' and 2D' modes.

These results suggest a high-content of graphitic carbon in produced nanomaterials. The measured signal was deconvoluted with a fitting routine comprising a Lorentzian peak for the D component, a BWF peak for the G component and a linear baseline with slope m . The resulting values of I_D/I_G intensity ratio, around 1.15, and m/I_G , around $1.9 \mu\text{m}$, are the typical signature of a highly graphitic material characterised by a low hydrogen content, further corroborating the previously described TEM analysis. The graphitic nanoparticles, produced in the particle generation cell, were dosed in the primary plasma during the Langmuir probe scans in dust-rich conditions. While, as described in the experimental section, the probe tip was cleaned after every measurement to prevent an excessive accumulation of nanoparticles at the probes surface, the particle accumulation at the tip during the I - V scans could still impair the reliability of measurements. To verify that the perturbations arising from the growth of a nanoparticle coating on the probe tip could, as a first approximation, be considered negligible we performed three

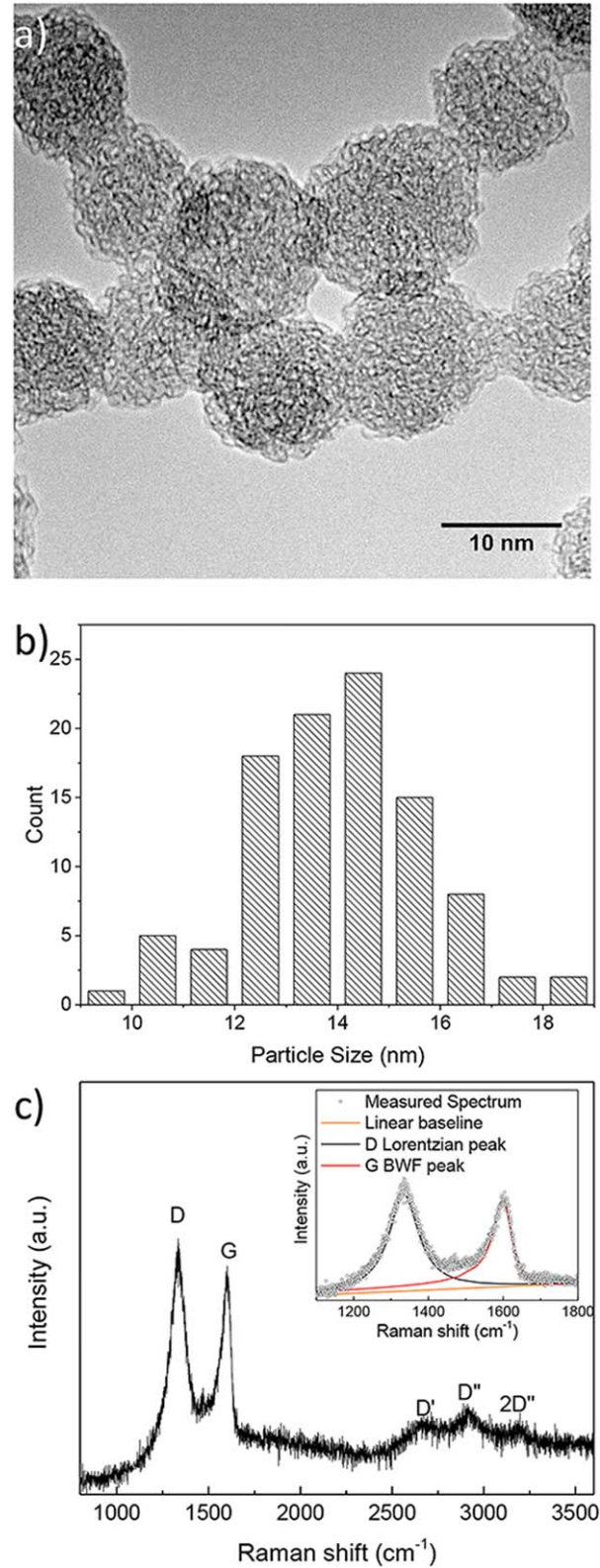


Figure 2. (a) High magnification TEM scan and (b) particle size distribution of the carbon nanomaterials produced by the nanoparticle generation cell. (c) Corresponding Raman spectrum of the synthesised materials (the deconvolution routine employed for the calculation of the I_D/I_G and m/I_G ratios is depicted in the inset).

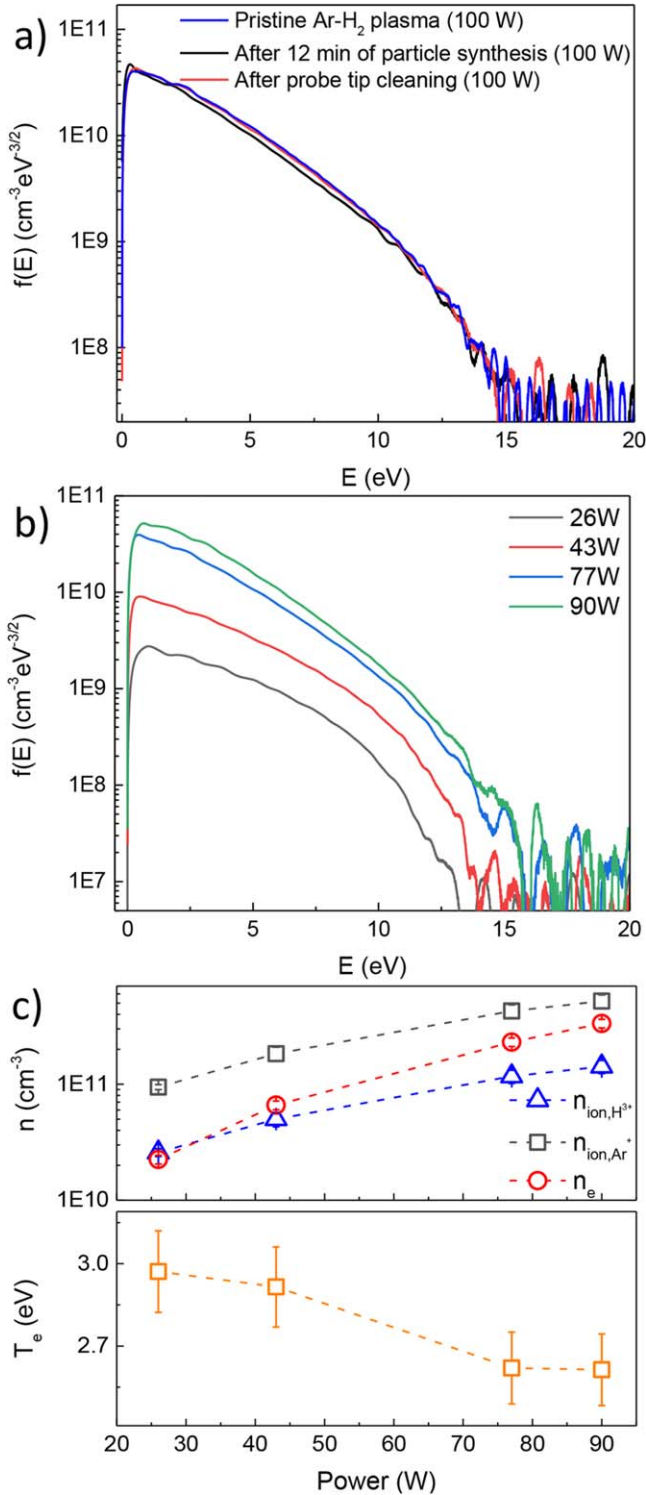


Figure 3. (a) $f(E)$ measurements taken for a dust free Ar-H₂ before particle injection, directly after 12 min of particle injection, and after cleaning the probe surface via electron bombardment. Notably, the nanoparticle generation cell was operated for a time significantly longer (12 min) than the one required for a single Langmuir probe measurement (3 min). (b) $f(E)$, (c) n_{ion} , n_e and T_e measured in a pristine Ar-H₂ plasma for increasing plasma powers.

experiments. We measured $f(E)$ in a dust-free Ar-H₂ with fixed RF input power before particle injection, directly after 12 min of carbon particle injection, and after cleaning the

probe surface via electron bombardment. The results are illustrated in figure 3(a). No major changes were observed in terms of $f(E)$, T_e , n_e , or n_{ion} for the three conditions.

The properties of the dust-free Ar-H₂ plasma as a function of applied RF input power were then investigated in the dust-free regime. The results for $f(E)$ are depicted in figures 3(b) and (c) shows n_{ion} , n_e and T_e as a function of RF input power. n_{ion} was calculated from equation (3) reported in the experimental session. Its value depends on the ion atomic mass m_{ion} . This introduces difficulties, since the dominant ion in an Ar-H₂ mixture is not known *a priori*, and the precise determination of the ion density is necessary to reliably obtain the nanoparticle charge using equation (5). Two primary ions are identified in the related literature as the most likely dominating species: Ar⁺ and H₃⁺ [22–24]. For the composition utilised in this investigation (with a 2% H₂ volume fraction), and based on both experimental and theoretical studies on non-thermal plasmas generated in this mixture, Ar⁺ is expected to be the dominant ion. Nevertheless, H₃⁺ may contribute significantly to the probe current in the ion saturation regime because of its lower atomic mass and higher electrical mobility.

In order to establish which ion mass is more appropriate to use for the determination of the ion density, we have first performed measurement in a pure argon plasma (results not shown here for brevity), confirming that the ion and electron densities obtained using equations (2) and (3) are close (within 20%) of each other. We have then performed measurements in the Ar-H₂ system as a function of the RF power. In figure 3(c) we report the electron density calculated using equation (2) and the ion densities calculated using equation (3) assuming an ion atomic mass corresponding to Ar⁺ and H₃⁺ respectively. At low RF power, for a plasma density lower than $5 \times 10^{10} \text{ cm}^{-3}$, the electron density is close to the ion density value obtained using the ion mass of H₃⁺. At higher power the electron density value approaches the ion density calculated using the Ar⁺ mass. In agreement with the related theory, as the plasma power is increased, the electron temperature, also shown in figure 3(c), decreases [25]. We point out that the nanoparticle heating models discussed in the literature, when dealing with particles immersed in an argon-hydrogen plasma, often assumes that the dominant ion is argon, i.e. the energy released to the particle by a charge recombination event corresponds to the ionisation potential of argon [26, 27]. Our experimental observation suggest that it would be more appropriate to assume that the heat flux is due to H₃⁺ recombination.

The properties of the Ar-H₂ plasma as a function of the RF power were investigated upon injection of the graphitic nanoparticles from the particle generation cell. Figures 4(a) and (b) report the measured $f(E)$, n_{ion} , n_e and T_e as a function of the power coupled in the primary plasma. H₃⁺ is assumed to be the dominant ion in the dust-rich plasma, since both the electron and ion density are low (well below $5 \times 10^{10} \text{ cm}^{-3}$). The dust density in the plasma is calculated from the material mass production of the particle generation cell, 1.6 mg h^{-1} ,

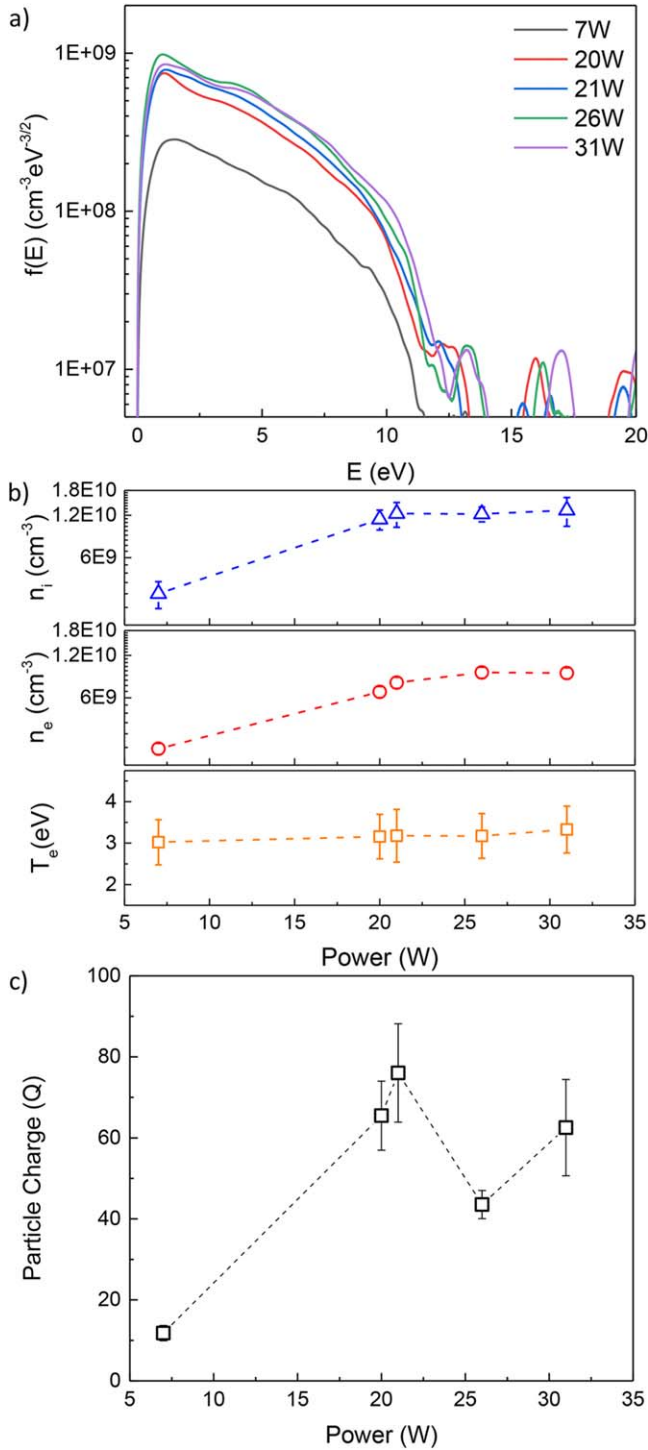


Figure 4. (a) $f(E)$ collected across a range of increasing plasma power in a dust rich Ar–H₂ plasma. (b) Corresponding n_{ion} , n_e and T_e for increasing plasma power. (c) Variation of number of negative charges per particle as a function of the plasma power.

and is highly dependent on the assumed material density. If we assume that the particles have a density corresponding to that of bulk graphite, 2.267 g cm^{-3} [28] the nanoparticle density is $7.3 \times 10^7 \text{ cm}^{-3}$. On the other hand, although Raman suggest their graphitised structure, TEM indicates that their morphology resembles that of crumpled graphene, whose density is likely much lower than that of graphite. Due

to a lack of precise density values for this case, we assume the density of amorphous carbon, 1.4 g cm^{-3} [28], and find that the corresponding nanoparticle density is $1.2 \times 10^8 \text{ cm}^{-3}$. We expect the nanoparticles density to fall between these two limiting cases.

From figure 4(b), the trend in ion density points to the presence of nanoparticles having a deep effect on the power coupling to the discharge. The energy distributions shown in figure 4(a) are similar to those shown in figure 3(b) for the low power limiting case. Although the electrical power is supplied to the reactor via a three-turn planar coil, the plasma in the pristine case is likely operating in a capacitively coupled mode at such low input powers. The low plasma density and relatively high electron temperature in the low power regime (see figure 3(c)) are consistent with this observation. We therefore conclude that the discharge is operating in capacitive mode for the dusty plasma case as well. We have found that any attempt at further increasing the input power for the dusty plasma case only leads to the onset of instabilities which are easily distinguishable by naked eye (rapid flickering of the plasma emission). We have found that the Langmuir probe measurement is impossible to perform while these instabilities are present because of wide fluctuations in current. The instabilities are clearly induced by the presence of dust, as observed by several other research groups [29–31], since it is trivial to operate the pristine plasma at significantly higher input power levels, as demonstrated by the energy distributions and by the plasma densities reported in figure 3. For the dusty plasma case, an increase in nanoparticle density, which can be achieved by increasing the acetylene flow rate to the secondary nanoparticle-producing plasma, only exacerbates this problem, i.e. facilitates the onset of instabilities.

The electron temperature in the dusty plasma case (figure 4(b)) is slightly higher than in the pristine case, in the low plasma input power regime (figure 3(c)). The presence of dust is expected to lead to an increase in electron temperature compared to the pristine case because of additional loss of ion-electron pairs to the particles surface. So while this relatively low electron temperature in the dusty plasma case may seem surprising, we should stress that the nanoparticle density is relatively low and an order of magnitude lower than the electron density. As already stated earlier, any attempt at increasing the nanoparticle density only resulted in the onset of instabilities that make the operational window of the discharge particularly narrow.

The presence of dust is confirmed by the fact that the ion density exceeds the electron density, as shown in figure 4(b). In figure 4(c) we plot the number of elementary negative charges per particle as a function of electrical power input. The number of charges per particle does not monotonically increase with power, instead reaches a maximum around 20 W to then decrease at higher input power.

To better clarify the origin of this behaviour, we have compared the measured plasma properties with a self-consistent steady-state zero-dimensional model for low-pressure argon plasmas containing nanoparticles which is solved numerically. At this time, hydrogen has not been included in the model for

simplicity. An additional simplification has been done in assuming that the electron energy distribution is Maxwellian. The model comprises four equations (7)–(10) which are well accepted as appropriate descriptors of particle charging in plasmas [32]. Equation (7) is based on the orbital-motion-limited theory and describes the collision frequency between charged species and particles $v_{e,\text{ion}}$:

$$v_{e,\text{ion}} = \begin{cases} n_{e,\text{ion}} S \sqrt{\frac{k_B T_{e,\text{ion}}}{2\pi m_{e,\text{ion}}}} \exp\left(-\frac{q_{e,\text{ion}} \Phi}{k_B T_{e,\text{ion}}}\right), & q_{e,\text{ion}} \Phi \geq 0 \\ n_{e,\text{ion}} S \sqrt{\frac{k_B T_{e,\text{ion}}}{2\pi m_{e,\text{ion}}}} \left(1 - \frac{q_{e,\text{ion}} \Phi}{k_B T_{e,\text{ion}}}\right), & q_{e,\text{ion}} \Phi \leq 0 \end{cases}, \quad (7)$$

where r_p is the particle radius, $S = 4\pi r_p^2$ is the particle surface area, $\Phi = \frac{Z_k}{4\pi\epsilon_0 r_p}$ is the particle potential, $Z_k = k \cdot e$ is the particle charge (e being the electron elementary charge and k is number of elementary charges carried), $n_{e,\text{ion}}$ is the electron (ion) density, $m_{e,\text{ion}}$ is the electron (ion) mass, k_B is the Boltzmann constant, $T_{e,\text{ion}}$ the electron (ion) temperature, and $q_{e,\text{ion}}$ is the respective electron (ion) charge. Equation (8) describes the quasi-neutrality of the discharge:

$$n_e + kn_{\text{particle}} = n_{\text{ion}}. \quad (8)$$

Equation (9) describes the ionisation balance and takes into account ion production by electron-induced ionisation and ion loss to the walls and to the particles

$$n_e v_{\text{ionization}} V = n_{\text{ion}} \left(\frac{D_a}{l}\right) A + n_p v_{\text{ion}} V, \quad (9)$$

where l is the characteristic diffusion length, D_a is the ambipolar diffusion length, $v_{\text{ionization}}$ stands for total ionisation frequency, V is the plasma volume, and A is the surface area bounding the plasma volume. $v_{\text{ionization}}$ results from the direct integration of the Ar ionisation cross-section over the electron energy distribution:

$$v_{\text{ionization}} = \langle N\sigma_{\text{ion}} U_{\text{th}} \rangle,$$

where N is the argon gas density at 300 K and at a pressure of 150 mTorr, U_{th} is electron thermal velocity and σ_{ion} is the ionisation cross-sections.

Equation (10) describes the power balance in the plasma discharge and takes into account the power provided by RF field as well as power loss to excitation and ionisation events in the discharge volume, power loss due to ion acceleration through the sheath, through electron-neutral momentum transfer, and to the nanoparticles through the collection of electrons.

$$\begin{aligned} P_{\text{rf}} &= n_e v_{\text{ex}} E_{\text{ex}} V + n_e v_{\text{ionization}} E_{\text{ion}} V + n_{\text{ion}} \left(\frac{D_a}{l}\right) \\ &\times A \left(\frac{V_{\text{sh}}}{2}\right) + \left(\frac{2m_e}{m_{\text{ion}}}\right) \frac{3}{2} k_B (T_e - T_g) n_e v_m V \\ &+ n_p V \int_{-\Phi}^{\infty} E e d v_e(\Phi, f_0, E), \end{aligned} \quad (10)$$

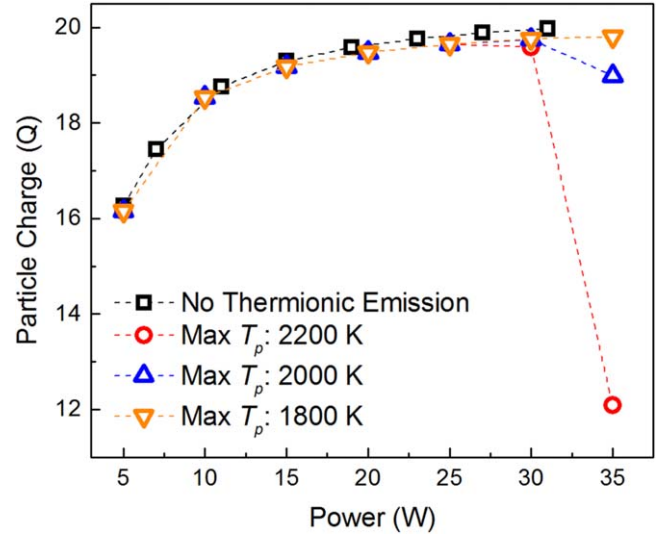


Figure 5. Variation of the number of negative charges per particle as a function of the plasma power obtained from the self-consistent model by employing the density of graphitic carbon. Thermionic emission is included in the model, T_p is the assumed maximum nanoparticle temperature.

where P_{rf} is the RF power, $v_{\text{ex}} = \langle N\sigma_{\text{ex}} U_{\text{th}} \rangle$ is the total excitation frequency, $v_m = \langle N\sigma_m U_{\text{th}} \rangle$ is the total momentum transfer frequency, E_{ex} is the effective electronic excitation energy, E_{ion} is the ionisation energy, and T_g is the Argon gas temperature (300 K). The collision cross sections are taken from the JILA database [33].

We also account for thermionic emission by including an emission frequency into the nanoparticle charge balance. The thermionic emission frequency which is described by Richardson's law in equation (11):

$$v_{\text{th}} = S \left(\frac{1}{e}\right) A_0 T_p^2 \exp\left(-\frac{W}{k_B T_p}\right), \quad (11)$$

where v_{th} stands for thermionic emission frequency, T_p is the particle temperature, $A_0 = \frac{4\pi m_e k_B^2 e}{h^3}$ is the Richardson constant, h stands for Planck's constant, and W is the work function (4.6 eV for graphitic carbon). The particle temperature is assumed to vary linearly with input power, from 300 K at 5 W to maximum temperatures of 1800, 2000 and 2200 K at 35 W.

The results from this self-consistent model are shown in figure 5. The nanoparticle size and density, based on the experimental values, are 14 nm and $1.6 \times 10^8 \text{ cm}^{-3}$. In figure 5, we plot the number of elementary charges carried by the particles as a function of input power, which increases slightly from 16 to 20. Considering the thermionic emission effect, a stark drop in particle charge at high particle temperatures is observed.

4. Conclusions

We have developed a test-bed for the characterisation of non-thermal plasmas which are controllably dosed with

nanoparticles independently produced in a secondary reactor. This approach allows investigating the properties of a dusty plasma which is completely decoupled from the kinetics of nucleation and growth. As an example, we have applied this approach to the case of an Ar–H₂ non-thermal plasma dosed with graphitic carbon nanoparticles, and investigated how input RF power affects parameters such as ion and electron density, electron temperature, and average particle charge. We have used a Langmuir probe for plasma characterisation, and found that this two-plasma reactors approach leads to a situation that is quite forgiving with respect of probe surface contamination. We have also found that while this approach allows accessing, in principle, a broad experimental parameters space, in reality the onset of dust-triggered plasma instabilities limits the actual range of parameters in which the characterisation can be successfully performed. Nevertheless, the results from this first study suggest that the power coupling to the discharge is severely affected by the presence of dust. As RF power is increased, the charge carrier density does not continuously increase, and the average nanoparticle charge decreases even at moderate input power. This behaviour cannot be captured by a particle charging model which is based on a simple, yet broadly utilised, set of governing equations. Additional assumptions on possible mechanisms that can lead to loss of negative charges, such as thermionic emission, are needed to qualitatively capture the experimental observations. These results suggest that the details of plasma-nanoparticle interaction are far from fully understood.

Acknowledgments

This work was supported by the US Department of Energy, Office of Science, Early Career Research Program under Award No. DESC0014169.

ORCID iDs

Lorenzo Mangolini  <https://orcid.org/0000-0002-0057-2450>

References

- [1] Selwyn G S, Singh J and Bennett R S 1989 *J. Vac. Sci. Technol. A* **7** 2758–65
- [2] Selwyn G S, Heidenreich J E and Haller K L 1991 *J. Vac. Sci. Technol. A* **9** 2817–24
- [3] Kortshagen U R, Sankaran R M, Pereira R N, Girshick S L, Wu J J and Aydil E S 2016 *Chem. Rev.* **116** 11061–127
- [4] Mariotti D and Sankaran R M 2010 *J. Phys. D: Appl. Phys.* **43** 323001
- [5] Alvarez Barragan A, Ilawe N V, Zhong L, Wong B M and Mangolini L 2017 *J. Phys. Chem. C* **121** 2316–22
- [6] Zhang H, Zhang R, Schramke K S, Bedford N M, Hunter K, Kortshagen U R and Nordlander P 2017 *ACS Photon.* **4** 963–70
- [7] Kessler V, Gautam D, Hulser T, Spree M, Theissmann R, Winterer M, Wiggers H, Schierner G and Schmechel R 2013 *Adv. Eng. Mater.* **15** 379–85
- [8] Nava G et al 2017 *J. Mater. Chem. C* **5** 3725–35
- [9] Holman Z C, Liu C-Y and Kortshagen U R 2010 *Nano Lett.* **10** 2661–6
- [10] Thimsen E, Johnson M, Zhang X, Wagner A J, Mkhoyan K A, Kortshagen U R and Aydil E S 2014 *Nat. Commun.* **5** 5822
- [11] Barragan A A, Nava G, Wagner N J and Mangolini L 2018 *J. Vac. Sci. Technol. B* **36** 011402
- [12] Greco E, Nava G, Fathi R, Fumagalli F, Del Rio-Castillo A E, Ansaldo A, Monaco S, Bonaccorso F, Pellegrini V and Di Fonzo F 2017 *J. Mater. Chem. A* **5** 19306–15
- [13] Zhong L, Guo J and Mangolini L 2015 *J. Power Sources* **273** 638–44
- [14] Godyak V A, Piejak R B and Alexandrovich B M 1992 *Plasma Sources Sci. Technol.* **1** 36
- [15] Godyak V A, Piejak R B and Alexandrovich B M 1993 *J. Appl. Phys.* **73** 3657–63
- [16] Tsv K P, Dimitrova M, Ivanova P, Kovačič J, Gyergyek T, Dejarnac R, Stöckel J, Pedrosa M A, López-Bruna D and Hidalgo C 2016 *Plasma Sources Sci. Technol.* **25** 033001
- [17] Bilik N, Anthony R, Merritt B A, Aydil E S and Kortshagen U R 2015 *J. Phys. D: Appl. Phys.* **48** 105204
- [18] Sudit I D and Chen F F 1994 *Plasma Sources Sci. Technol.* **3** 162
- [19] Chatterton P A, Rees J A, Wu W L and Al-Assadi K 1991 *Vacuum* **42** 489–93
- [20] Druyvesteyn M J 1930 *Z. Phys.* **64** 781–98
- [21] Woodard A, Shojaei K, Nava G and Mangolini L 2018 *Plasma Chem. Plasma Process.* 683–94
- [22] Mason R S, Miller P D and Mortimer I P 1997 *Phys. Rev. E* **55** 7462–72
- [23] Bogaerts A and Gijbels R 2000 *J. Anal. At. Spectrom.* **15** 441–9
- [24] Laidani N, Bartali R, Tosi P and Anderle M 2004 *J. Phys. D: Appl. Phys.* **37** 2593
- [25] Lee H-C, Seo B H, Kwon D-C, Kim J H, Seong D J, Oh S J, Chung C-W, You K H and Shin C 2017 *Appl. Phys. Lett.* **110** 014106
- [26] Mangolini L and Kortshagen U 2009 *Phys. Rev. E* **79** 026405
- [27] Kramer N J, Anthony R J, Mamunuru M, Aydil E S and Kortshagen U R 2014 *J. Phys. D: Appl. Phys.* **47** 075202
- [28] Robertson J 1986 *Adv. Phys.* **35** 317–74
- [29] Mikikian M, Couëdel L, Cavarroc M, Tessier Y and Boufendi L 2007 *New J. Phys.* **9** 268
- [30] Pacha K A, Heinrich J R, Kim S H and Merlino R L 2012 *Phys. Plasmas* **19** 014501
- [31] Heinrich J R, Kim S H and Merlino R L 2011 *Phys. Rev. E* **84** 026403
- [32] Kortshagen U and Bhandarkar U 1999 *Phys. Rev. E* **60** 887–98
- [33] Yamabe C, Buckman S J and Phelps A V *Phys. Rev. A* **27** 1345